

Characteristics of Bi-metallic Interfaces Formed During Direct Energy Deposition Additive Manufacturing Processing



RYAN ANDERSON, JORDAN TERRELL, JUDY SCHNEIDER, SEAN THOMPSON,
and PAUL GRADL

Various additive manufacturing processes are being evaluated to reduce the time and cost for fabrication of low volume, complex, and multifunctional assemblies. This study evaluated two direct energy deposition processes for the fabrication of large bi-metallic structures. The materials evaluated were Inconel 625 and copper alloy C18150, which are used in various high heat flux applications. Inconel was deposited onto the C18150 substrate using blown powder and wire-fed processes. Complete bonding was obtained in both processes and the resulting interfaces were evaluated using microscopy and indentation testing. Differences were observed in the interface region suggesting the kinetic energy of the blown powder process resulted in more residual stress at the interface, promoting recrystallization and enhanced diffusion. This created a broader interface in the blown powder specimens compared to a narrower mechanically mixed interface with the wire-fed process.

<https://doi.org/10.1007/s11663-019-01612-1>

© The Minerals, Metals & Materials Society and ASM International 2019

I. INTRODUCTION

ADDITIVE manufacturing (AM) processes are being evaluated for reducing the fabrication time and costs in various applications. The ability to directly print complex shapes with internal features in difficult to machine alloys is making this an attractive alternative to traditional subtractive manufacturing which requires subsequent assembly of multiple parts. AM processes for metal use either powder bed fusion (PBF) or direct energy deposition (DED).^[1–3] Each process has their associated tradeoffs in terms of feature resolution and deposition rate. PBF printing has the highest resolution of feature size but is limited to slow deposition of monolithic components that fit within the powder box. In contrast, DED processes have lower feature resolution but are applicable to rapid deposition of larger scale components using multiple materials. DED processes

use an energy source, such as a laser or plasma arc to directly build a component from feedstock, which can be either powder or wire.

Several industries utilize bi-metallic material combinations in high heat flux applications.^[4–6] Often these designs include an outer nickel (Ni)-based superalloy, selected for strength at elevated temperatures, joined to a copper (Cu) alloy, selected for thermal conductivity. Using this material combination in regeneratively cooled combustion chambers and nozzles for liquid rocket engine applications requires fabrication of large structures.^[6] DED can print at these length scales and would greatly reduce the time and hence fabrication cost by eliminating multiple processing steps for one-step fabrication of bi-metallic components. However, little is known about the resulting interface formed as the metals are directly deposited on one another.^[7–9] This study characterizes the resulting bi-metallic interface formed between Inconel 625 and C18150 in specimens fabricated by two different DED processes. Characterization techniques include microscopy and indentation testing across the interface.

RYAN ANDERSON, JORDAN TERRELL, and JUDY SCHNEIDER are with the Department of Mechanical and Aerospace Engineering, University of Alabama in Huntsville, Huntsville, AL 35899. Contact e-mail: jas0094@uah.edu SEAN THOMPSON is with the US Army CCDC Aviation and Missile Center, Redstone Arsenal, AL 35898. PAUL GRADL is with the NASA Marshall Space Flight Center, Huntsville, AL 35812.

Manuscript submitted December 14, 2018.

Article published online May 31, 2019.

II. BACKGROUND

In all DED processes, the heat source can be co-mounted onto either a robotic arm or a computer numerical control (CNC) platform. This configuration increases the degrees of freedom available for the

deposition of material in the build. Typically, the heat source and feed system are fixed horizontally with the part rotating beneath the heat source.

Wire-fed DED processes can use either a pulsed plasma arc, as shown in Figure 1, or a pulsed laser as shown in Figure 2. A wire feedstock is fed into the path of the heat source, locally melting it to the substrate or prior layers.^[10] The wire diameters range from 0.2 to 4 mm with the smaller diameter wire deposited with a laser heat source and the larger with a pulsed plasma arc.

A blown powder system is illustrated in Figure 3, in which an inert gas delivers the powders through a nozzle to the focal point of the heat source, typically a laser, melting it to the substrate or prior layers. The system can be configured with multiple hoppers to deliver different powders through the nozzles for deposition.

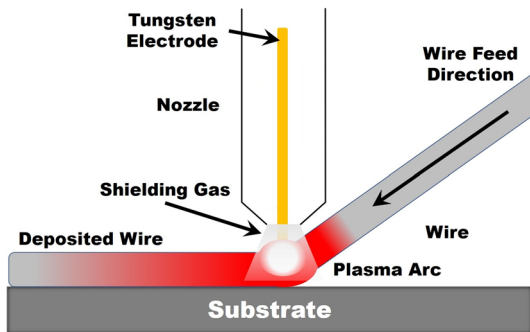


Fig. 1—Schematic of pulsed plasma arc wire-fed DED AM.

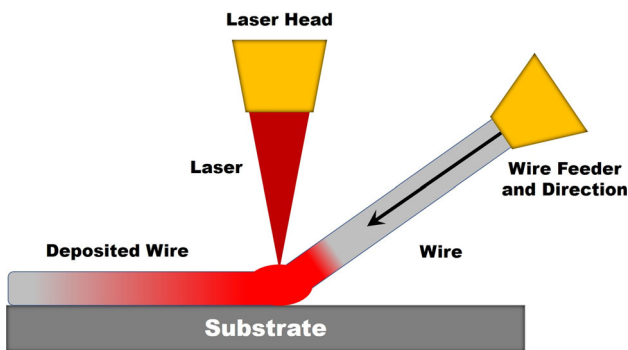


Fig. 2—Schematic of pulsed laser wire-fed DED AM.

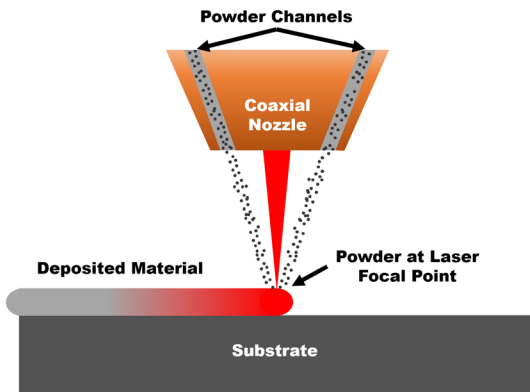


Fig. 3—Schematic of blown powder DED AM.

Several studies on AM of bi-metallics have evaluated the use of functionally graded transitions to mitigate the influence of intermetallic compounds or accommodate resulting residual stress concentrations. Blown powder processing is commonly used with multiple hoppers for the different materials, such as Titanium or Inconel to Stainless Steels.^[11–17] Due to the layering, this results in a transition zone width on the order of microns. While these materials have similar melting temperatures, there are differences in the thermal conductivity as well as the coefficient of thermal expansion. More recently, bi-metallic structures of Inconel to Cu alloys are being evaluated.^[7–9] These materials have similar differences in their thermophysical and mechanical properties with a greater difference in their melting range.

In applications of high heat fluxes, Cu alloy liners are reinforced with materials such as Inconel that retains its strength at high temperatures.^[4–6] In the binary Cu to Ni phase diagram, there is complete solubility with no intermetallic compounds.^[18] Although this bi-metallic combination provides the metallurgical compatibility for AM processing, there remains a large difference in thermophysical and mechanical properties. As this can result in residual stresses leading to cracks and delamination at the bond interface, methods to maintain an effective bond without cracking are needed.

A bi-metallic igniter was recently fabricated by NASA using a hybrid AM process and hot fire tested.^[9] This component used blown powder DED of an Inconel 625 structural jacket over a C18150 copper core with machined internal coolant passages. Preliminary metallography was completed to ensure bonding at the interface with no evidence of cracks. This study expands this topic to consider other DED processing routes. The materials used in this study are a Cu alloy (C18150) and a Ni-based superalloy (Inconel 625) whose elemental compositions are summarized in Table I. The primary elements of Cu and Ni are completely miscible and marketed under the trade name of Monel 400, which is 30 wt pct Cu and 70 wt pct Ni.

The Cu and Ni alloys used in this study have very different thermal and mechanical properties as summarized in Table II. Note the published values for the mechanical properties reflect the effect of the post-processing heat treatments for the C18150 which is precipitation strengthened and Inconel 625 which is mill annealed. As a laser energy source was used for both DED processes, the main difference in the deposition process is the effect of the carrier gas velocity used with the blown powder as compared to the wire fed.

III. EXPERIMENTAL PROCEDURE

The materials used in this study were Inconel 625, C18150, and Monel 400 whose elemental compositions are summarized in Table I and their properties summarized in Table II. Inconel 625 is a nickel (Ni)-based superalloy which predominately derives its strength from solid solution strengthening.^[19,22,23] C18150 is a copper-chromium-zirconium (Cu-Cr-Zr), precipitation-strengthened alloy.^[20]

Table I. Summary of Alloy Elemental Composition (Weight Percent)

Alloy	Ni	Cu	Cr	Zr	Mo	Nb	Al	Ti	Mn	Si
Inconel 625 ^[19]	61.0	—	21.5	—	9.0	3.6	0.2	0.2	0.2	0.2
C18150 ^[20]	—	Bal	0.5–1.5	0.02–0.20	—	—	—	—	—	—
Monel 400 ^[21]	≥ 63.0	28–34	—	—	—	—	—	—	≤ 0.90	≤ 0.50

Table II. Summary of Material Properties

Alloy	Yield Strength (MPa)	Ultimate Tensile Strength (MPa)	Hardness (Knoop)	Thermal Conductivity ($\frac{W}{mK}$)	Coefficient of Thermal Expansion (mm/(m °C))	Melting Range (°C)
Inconel 625 ^[19]	490	965	286	9.8	14.2	1290–1350
C18150 ^[20]	338–579	476–586	164–175	323	17.1	1070–1080
Monel 400 ^[21]	240	550	185	21.8	13.9	1300–1350

Table III. Sample Nomenclature

Sample Name	Sample Composition	Number of Samples
WF#1	C18150 + Ni flash + pulsed laser Inconel 625	14
WF#2	C18150 + Ni flash + pulsed laser Inconel 625 + pulsed arc Inconel 625	9
WF#3	C18150 + Ni flash + pulsed laser Monel 400 + pulsed laser Inconel 625	6
BP#1	C18150 + blown powder Inconel 625	7

Monel 400 is a Cu-Ni solid solution alloy.^[21] Due to the elemental composition consisting of the base elements of C18150 and Inconel 625, it was evaluated to form a functionally graded interface between the Cu and Ni alloys to promote mixing and diffusion. Due to the differences in the melting range for the materials evaluated, the specimens were evaluated in the as-built condition with no post-processing heat treatments applied.

Specimens were prepared for this study using wire-fed and blown powder Inconel 625 feedstock with a laser energy source as summarized in Table III. All samples deposited Inconel 625 directly onto a C18150 cylindrical substrate, with the exception of WF#3 which used a Monel 400 transition layer. With the wire-fed specimens, a 25 μm layer of commercially pure Ni was deposited onto the Cu substrate prior to depositing Inconel or Monel to minimize oxidation. The blown powder systems utilized a hybrid additive/subtractive AM system which allowed the Cu substrate to be machined prior to deposition to remove the oxides.

Initial attempts to deposit Inconel 625 directly to the Cu substrate using a pulsed plasma arc system resulted in poor bonding and were discontinued. The visual delamination was linked to the greater thermal energy of the pulsed arc combined with the larger mass of the wire feedstock. The thermal mass was reduced by using the pulsed laser as the heat source with the small-diameter wire feedstock in WF#1. Subsequent use of pulsed arc was used to rapidly build up the Inconel 625 deposition after the initial layers were completed with no evidence of debonding in WF#2.

After deposition trials, all samples were sectioned with an abrasive saw and subsequently mounted in phenolic for metallurgical preparation. Standard metallographic preparation was used to grind the samples with increasingly fine-grit silicon carbide (SiC) paper followed by polishing with 1 and 0.05 μm alumina (Al_2O_3). Optical microscopy images were collected using a Zeiss AXIO Vert.A1 Inverted Microscope and stitched together to form a montage of the interface.

Following initial optical imaging, the specimens were chemically etched to reveal the grain structure. Multiple etchants were used to coax the microstructures out of the different materials. The C18150 and Monel 400 were etched first using Waterless Kalling's Reagent although nitric acid was later found to be a better etchant. Next, Inconel was electro-etched using an oxalic solution. The resulting images were edited and the two etched halves were stitched together.

Knoop hardness tests evaluated variations across the interface in two representative samples. A Wilson Tukon 2100/Instron tester was used with a rhombic-based pyramidal-shaped diamond indenter under a load of 500 g. The test followed ASTM E384 and was taken across two representative samples, WF#3 and BP#1. Indents were made starting in the Cu portion and ended in the Inconel transitioning across the bi-metallic interface.

After recording optical microscopy images, the samples were repolished to remove the etchant for imaging in a Hitachi S-3700 scanning electron microscope (SEM) with Oxford Energy-Dispersive X-Ray Spectroscopy (EDS) for elemental mapping. The SEM/EDS images

were used to qualitatively identify the elemental composition and width of the interfaces formed. Grain sizes were based on the feret diameter for approximately 50 grains using ImageJ software for analysis.

IV. RESULTS AND DISCUSSION

Due to the immaturity of multi-material joining *via* AM, standards discussing visual inspection criteria for a “successful” joint do not exist. Brazing, a similar and vastly more mature joining process, uses a case-by-case inspection criteria determined by the component’s application.^[24] For this study, a bonding process is considered “successful” by qualitative visual inspection consistently showing little to no delamination between the parent alloys.

Figures 4, 5, 6, and 7 show the pre-etched interfaces. These images show complete bonding at the interface between the two alloys in all the methods. It also appears that the use of both pulse laser and plasma arc together in WF#2 and the use of Monel 400 were met with successful bonding. Upon further examination, the main characteristics of note are the differences in the interfaces. The wire-fed samples have abrupt changes from the Cu alloy to the Ni alloy, while the blown powder samples have a much broader interface between Cu and Ni. Initial observations suggest that the difference in the interfacial interaction occurs because of the physical characteristics inherent to the two forms of deposition. The wire-fed process simply “lays” the feedstock onto the substrate, whereas the velocity of the blown powder process “propels” the feedstock onto and into the substrate. Thus, it appears that different

types of interactions at the interface could be a result of the absence or presence of kinetic motion of feedstock deposition.



Fig. 5—Unetched interface of sample WF#2.

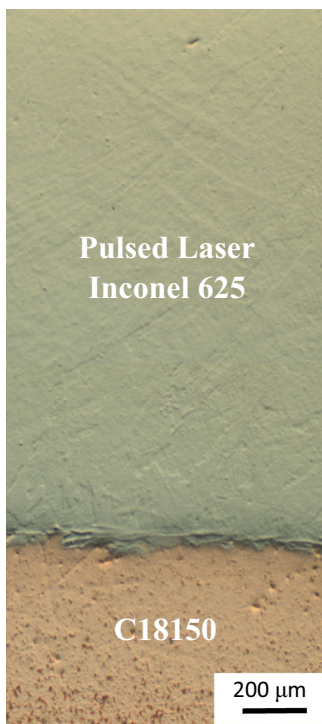


Fig. 4—Unetched interface of sample WF#1.



Fig. 6—Unetched interface of sample WF#3.

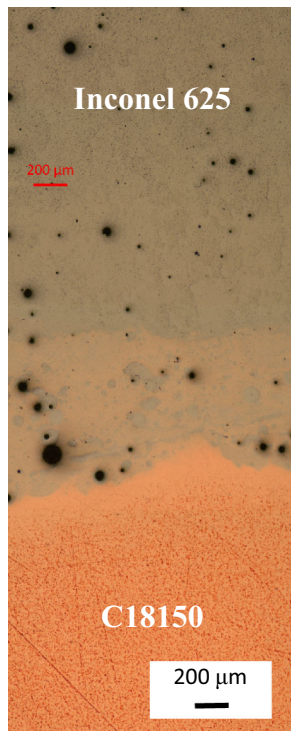


Fig. 7—Unetched interface of sample BP#1.

The etched images in Figures 8, 9, 10, and 11 highlight the differences between the two processes. The abruptness of the interface in the wire-fed samples compared with the broadness of the blown powder interface continues to appear after etching. The wrought C18150 microstructure displays many small grains which are typical of the wrought alloy, while the Inconel 625 grains appear to be both large and dendritic retaining features of the deposition process. At the interface between the weld patterns in WF#2, shown in Figures 5 and 9, it is apparent where the pulsed laser and pulsed plasma arc depositions meet. While all three of the wire-fed etched images show some interaction at the interface, WF#3 in Figures 6 and 10 show more perturbation along the interface in comparison to the other wire-fed samples. Since Monel 400 is a solid solution of Ni and Cu, per Table I, it has a higher affinity for the predominantly Ni Inconel 625 and the predominantly Cu C18150 than the two primary alloys have for one another. Thus, the perturbations appear to result from the use of Monel 400 as an intermediary alloy that facilitate better diffusional mixing between the Cu and Ni alloys in comparison to WF#1 and WF#2.

A close up of the blown powder interface from Figure 11 is shown in Figure 12. With the blown powder DED process, a 1-mm-wide interface forms contrasting with the sharp interface in the wire-fed DED process. The C18150 had initial grain diameters in the range of 30 to 45 μm . Within the interface region shown in Figure 12, there are regions of unmelted Inconel particles surrounded by small Cu grains. These Cu grains have diameters of $8 \pm 2 \mu\text{m}$ indicated within the circled regions. Also noted by arrows are regions of

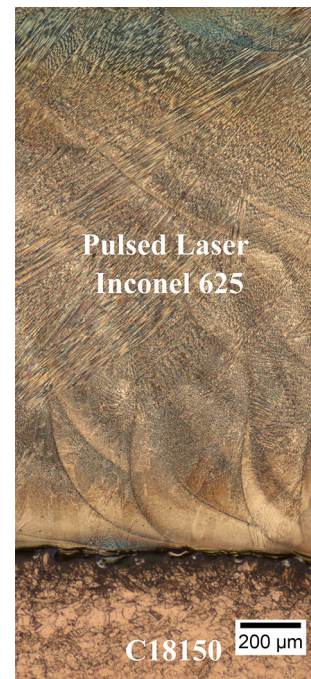


Fig. 8—Etched interface of sample WF#1.

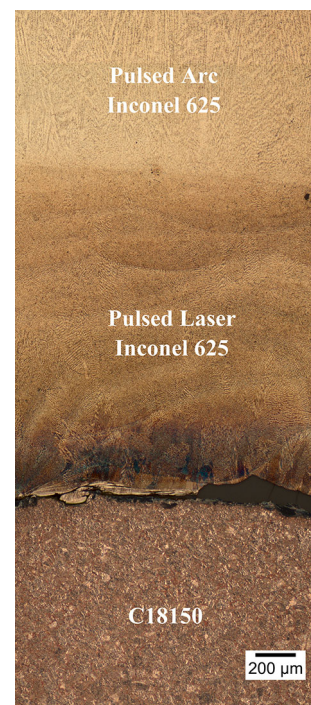


Fig. 9—Etched interface of sample WF#2 (note dark region at the interface is an etching artifact).

dendrites. A close up of a representative dendritic region is shown in Figure 13. These differences in the interface regions observed further substantiate the hypothesis that the inherent difference of feedstock deposition results in different bonding mechanisms for the wire-fed DED vs the blown powder DED.

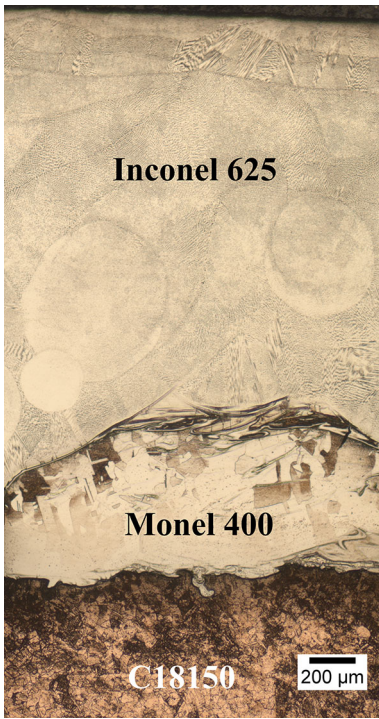


Fig. 10—Etched interface of sample WF#3.

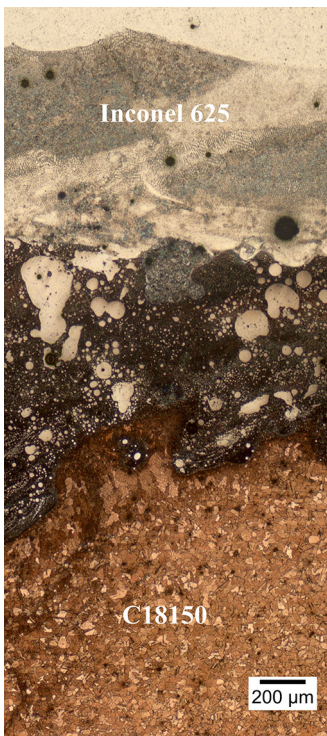


Fig. 11—Etched interface of sample BP#2.

The Knoop hardness data taken across the interface of the as-deposited specimens are shown in Figures 14 and 15. Since both Inconel 625 and Monel 400 are solid solution strengthened, their hardness values are within the published range. However, since the C18150 did not

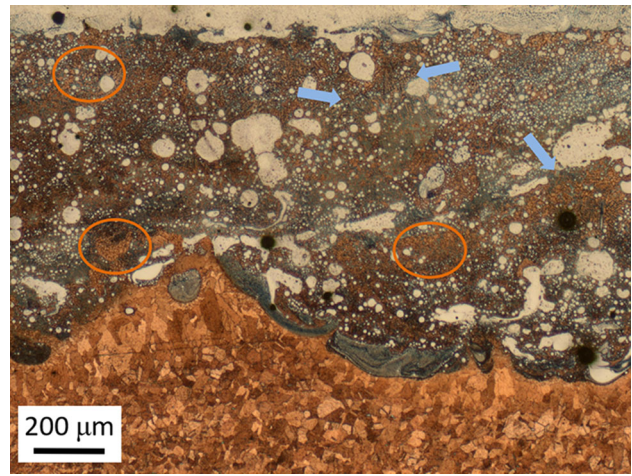


Fig. 12—BP#1 enlarged image of the interface, ellipses emphasize Cu grains within the interface, and arrows indicate locations of dendrites. A closeup of the dendritic structure is provided in Fig. 13.

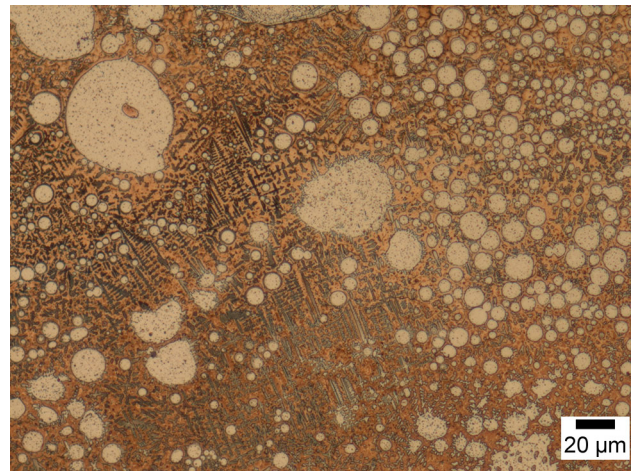


Fig. 13—Close up image of dendritic region observed at the interface in Fig. 12.

undergo a precipitation heat treatment, its hardness is noticeably lower than fully aged wrought values. Comparing Figures 14 and 15, a difference is noted across the interface region. Both graphs have a “stair step” appearance. While this would be expected for Figure 14 as it consists of three different alloys, Figure 15 has only two alloys. In Figure 14, the hardness abruptly increases as the indenter crosses from the Cu into Monel and from Monel into Inconel. The first measurement in the Inconel section is slightly softer than the rest of the Inconel. This discrepancy was resolved by discovering the indenter tested a region where bands of Inconel and Monel interacted. Figure 15 has only the Cu and Inconel alloys, but as the indenter crossed from Cu into the interfacial zone, the hardness increases, indicating more than just the Cu alloy exists in this zone. The presence of more Inconel or Ni itself could improve hardness through solid solution strengthening. The hardness increases again as it crosses from the interface zone into the Inconel region. One discrepancy in

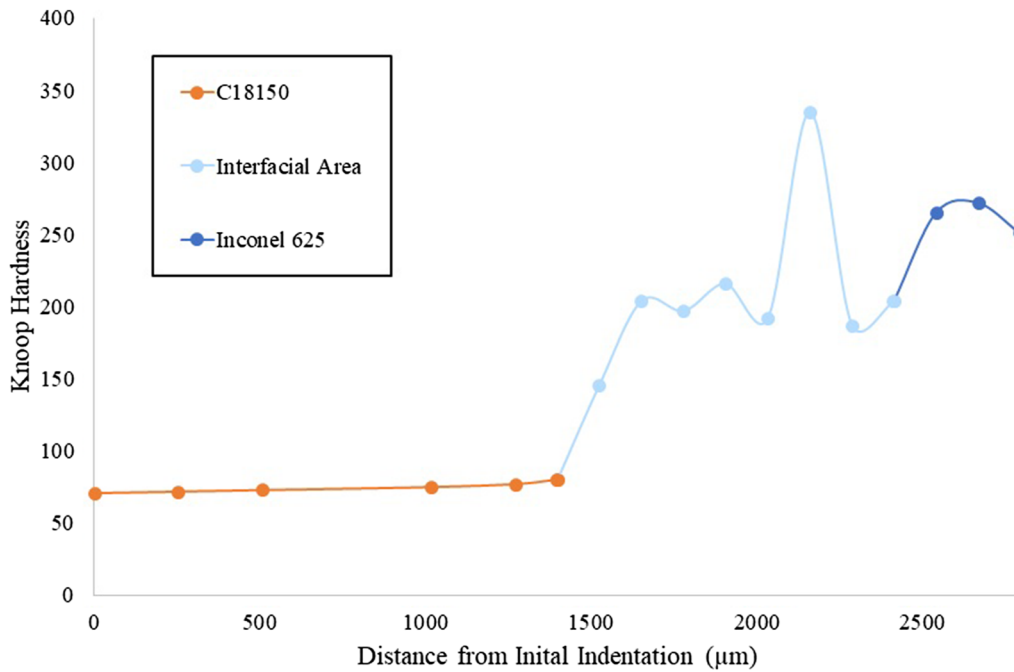


Fig. 14—Knoop hardness plot across interface of WF#3.

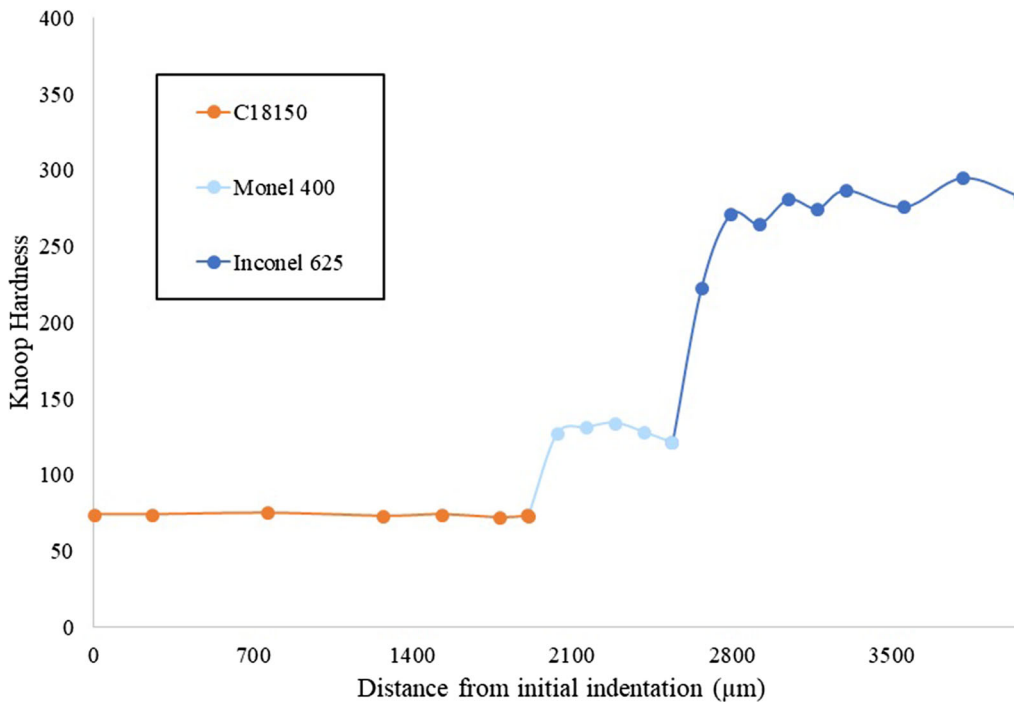


Fig. 15—Knoop hardness plot across interface of BP#1.

Figure 15 is the “spike” in hardness in the middle of the interfacial zone. Examining the indentation site revealed that the indenter struck an Inconel particle. These data appear to confirm the assumption that two different mechanisms are occurring at the interfaces of the wire-fed and blown powder samples.

The elemental maps created from the SEM/EDS scans are shown in Figures 16, 17, and 18. Figure 16 shows that the wire-fed interface in WF#2 between Cu and Ni does not penetrate, but rather they appear to have small “bands” mechanically locking with each other. This suggests the interface formation was only driven by the

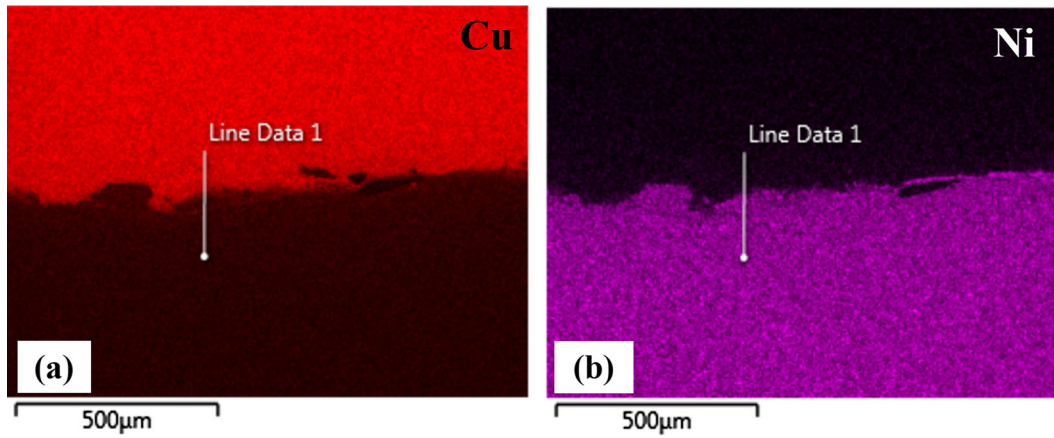


Fig. 16—EDS elemental map of sample WF#2, (a) Cu elemental map, (b) Ni elemental map (Note “Line Data 1” is an unremovable object and is not discussed in this paper).

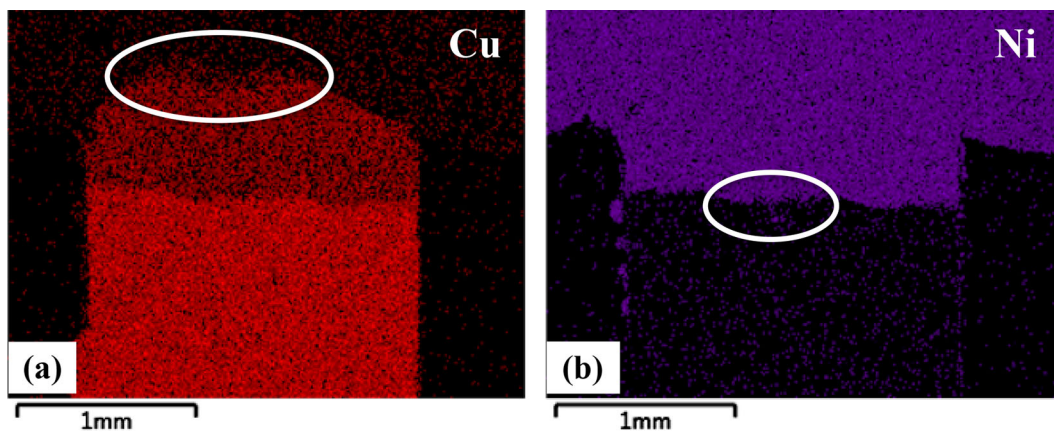


Fig. 17—EDS elemental map of specimen WF#3 with ellipses to emphasize mixed interfaces, (a) Cu elemental map, (b) Ni elemental map.

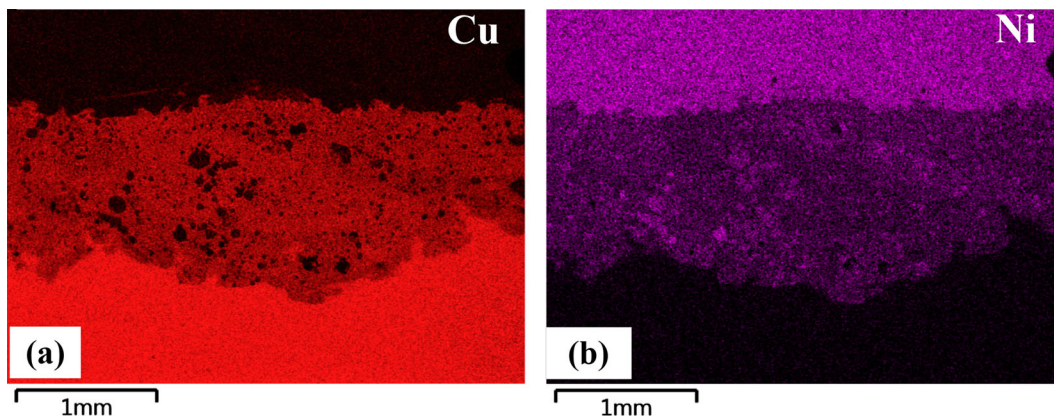


Fig. 18—EDS elemental map of specimen BP#1, (a) Cu elemental map, (b) Ni elemental map.

thermal energy and the pulsing of the heat source at the bi-metallic interfaces. The elemental maps for WF#3 show additional mixing at the interface which is indicated by the less abrupt boundaries, highlighted within the ellipses regions in Figure 17, showing higher

interaction of the primary elements of all three alloys. This can also give credence to the drop in hardness in Figure 14 at the start of the Inconel section. The indenter appeared to test an area where bands of Inconel and Cu were interacting. The maps further

indicate that the intermediate Monel 400 alloy facilitates greater mixing due to the higher affinity of the parent alloys for Monel 400 than they have for each other.

Figure 18 shows a qualitatively more even distribution of Cu and Ni in the interfacial zone, which implies a greater degree of diffusion. Similarly, the maps reinforce the enhanced interaction between alloys in the blown powder DED process than in the wire-fed DED process due to the width of the elemental interaction area of Figure 18 in comparison to Figures 16 and 17. The elemental maps also provide evidence that the particles suspended in the interface are Inconel particles as indicated by high concentration of Ni. This further corroborates the belief that the hardness spike in Figure 15 was caused by the indenter tip measuring the hardness of an Inconel particle.

In the blown powder process, Inconel impacts the Cu substrate at a higher velocity than the wire-fed processes. Although the velocity is much less than is necessary in cold spray processing,^[25] a similarly “blown” metal deposition process, the momentum of the blown powder could still result in increased residual stress at the interface. Stress concentrations have been reported to be an important step in the nucleation of new grains.^[26–28] Also, atomic transport phenomenon is known to be faster along grain boundaries than through the crystal or the bulk of the grains.^[29,30] Therefore, by increasing the local residual stress, diffusion-induced recrystallization (DIR) can occur resulting in a higher diffusion rate.^[26] An increased diffusion rate could help produce the wider interface observed in the blown powder samples. Figure 12 provided a closer look at the microstructure of the C18150 and the diffusion zone in which trapped Inconel 625 particles mixed with the recrystallized Cu grains. Smaller grains of Inconel are also observed at the edge of the diffusion zone in the top right corner of Figure 12. The presence of these smaller grains further substantiates the occurrence of DIR in the interface and suggests the effects of DIR are extending further into the parent alloys. The evidence of DIR, the wide area of qualitatively even distribution of Cu and Ni in Figure 18, and the hardness change through this same wide area all indicate that this blown powder DED process between Inconel 625 and C18150 creates a wider diffusion zone at the interface of the two alloys.

In the wire-fed samples, the Cu grains at the interface do not appear to recrystallize but rather grow due to the absence of residual stress when Cu comes in contact with the molten Inconel. This results in an interface that is abrupt with no grain size reduction. With less grain boundaries, the diffusion process is slower. The combination of these characteristics, as well as the SEM EDS imaging and the Knoop hardness tests, means the primary bonding mechanism is not diffusion dominated but is driven by the pulsing action of the laser as it melts both the feedstock and the surface of the C18150 alloy.

Thus, the kinetic energy of the blown powder DED combines with the thermal energy to creating a broad, diffusion interface, while the wire-fed DED only has thermal energy available for mixing with the Cu surface.

V. SUMMARY

This study showed successful bi-metallic bonds can be created using both wire-fed and blown powder DED AM processes. In both cases, complete bonding was obtained as evidenced by no observed delamination. However, the pulsed-laser, wire-fed AM samples tend to favor mechanical mixing of the alloys, while the blown powder AM samples tend to favor diffusion bonding. Although the interface has been characterized using SEM EDS and optical microscopy, further study of the bonds will include inspection for intermetallics present using X-Ray diffraction and transmission electron microscopy in addition to evaluating the mechanical property differences using mechanical testing.

ACKNOWLEDGMENTS

This work was supported in part from NASA STTR Phase I with Keystone Synergistic Enterprises, Inc. Grant No. NNX16CM41P, “Advancing Metal Direct Digital Manufacturing (MDDM) Processes for Reduced Cost Fabrication of Bi-Metallic Cooled Rocket Engines,” and Aetos Systems Grant No. NNM14AA15C/Subcontract No. 2019. A52, “Additive/subtractive manufacturing of combustion devices.”

REFERENCES

1. W.E. Frazier: *JMEPEG*, 2014, vol. 23, pp. 1917–28. <https://doi.org/10.1007/s11665-014-0958-z>.
2. W.J. Sames, F.A. List, S. Pannala, R.R. Dehoff, and S.S. Babu: *Int. Mater. Rev.*, 2016, vol. 61 (5), pp. 315–60. <https://doi.org/10.1080/09506608.2015.1116649>.
3. A. Bandyopadhyay and K.D. Traxel: *JAM*, 2018, vol. 22, pp. 758–74.
4. V.V. Rybin and D.L. Smith: *J. Nucl. Mater.*, 1992, vols. 191–194, pp. 30–36.
5. J.M. Kazaroff and G.A. Repas: *NASA Technical Paper No. 2694*, 1987.
6. P.R. Gradl: 2016, *AIAA Conf. Proc. No. 2016–4771*. <https://ntrs.nasa.gov/archive/nasa/casi.ntrs.nasa.gov/20160009709.pdf>. Accessed 22 March 2017.
7. A. Bandyopadhyay and B. Heer: *Mater. Sci. Eng. Rev.*, 2018, vol. 129, pp. 1–16.
8. B. Onuikwe, B. Heer, and A. Bandyopadhyay: *JAM*, 2018, vol. 21, pp. 133–40.
9. NASA-MSFC Press Release, https://www.nasa.gov/centers/mars_hall/news/news/releases/2017/nasa-tests-first-3-d-printed-rocket-engine-part-made-with-two-different-alloys.html. Accessed 19 September 2017.
10. S.W. Williams, F. Martina, A.C. Addison, J. Ding, G. Pardal, and P. Colegrove: *Mater. Sci. Tech.*, 2016, vol. 32 (7), pp. 641–47.
11. D.C. Hofmann, J. Kolodziejska, S. Roberts, R. Otis, R.P. Dillon, J.O. Suh, Z.K. Liu, and J.P. Borgonia: *J. Mater. Res.*, 2014, vol. 29 (17), pp. 1899–1910.
12. K. Shah, I. Ul Haq, A. Khan, S.A. Shah, M. Khan, and A.J. Pinkerton: *Mater. Des.*, 2014, vol. 54, pp. 331–38.
13. H. Sahasrabudhe, R. Harrison, C. Carpenter, and A. Bandyopadhyay: *JAM*, 2015, vol. 5, pp. 1–8.
14. A. Hinojos, J. Mireles, A. Reichardt, P. Frigola, P. Hosemann, L.E. Murr, and R.B. Wicker: *Mater. Des.*, 2016, vol. 94, pp. 17–27.
15. B.E. Carroll, R.A. Otis, J.P. Borgonia, J.-O. Suh, R.P. Dillon, A.A. Shapiro, D.C. Hofmann, Z.-K. Liu, and A.M. Beese: *Acta Mater.*, 2016, vol. 108, pp. 46–54.

16. A. Reichardt, R.P. Dillon, J.P. Borgonia, A.A. Shapiro, B.W. McEnerney, T. Momose, and P. Hosemann: *Mater. Des.*, 2016, vol. 104, pp. 404–13.
17. W. Li, S. Karnati, C. Kriewall, F. Liou, J. Newkirk, K.M. Brown-Taminger, and W.J. Seufzer: *JAM*, 2017, vol. 14, pp. 95–104.
18. Phase Diagrams. European Space Agency. http://www.spaceflight.esa.int/impress/text/education/Solidification/Phase_Diagrams.html#Top. Accessed 5 November 2016.
19. Haynes International Brochure H-3073D, <http://mail.haynesintl.com/pdf/h3073.pdf>. Accessed August 2018.
20. <https://alloys.copper.org/alloy/C18150>. Accessed 5 September 2017.
21. Special Metals MONEL® Alloy 400. MatWeb: Material Property Data. <http://www.matweb.com/search/datasheet.aspx?matguid=1364d8231703476b8c466cdd07be71b7>. Accessed 16 October 2017.
22. H. L. Eiselstein and D. J. Tillack: *TMS pub.*, 1991, <https://doi.org/10.7449/1991/superalloys> 1991, pp. 1–14.
23. A.K. Jena and M.C. Chaturvedi: *J. Mater. Sci.*, 1984, vol. 19, pp. 3121–39.
24. American Welding Society C3 Committee on Brazing and Soldering: *Brazing Handbook*, 5th ed., American Welding Society, Miami, FL, 2007, pp. 169–78.
25. S. Yin, P. Cavaliere, B. Aldwell, R. Jenkins, H. Liao, W. Li, and R. Lupoi: *JAM*, 2018, vol. 21, pp. 628–50.
26. S.M. Schwarz, B.W. Kempshall, and L.A. Giannuzzi: *Acta Mater.*, 2002, vol. 51 (10), pp. 2765–76. [https://doi.org/10.1016/S1359-6454\(03\)00082-X](https://doi.org/10.1016/S1359-6454(03)00082-X).
27. H.L. Wang, Z.B. Wang, and K. Lu: *Acta Mater.*, 2011, vol. 59, pp. 1818–28.
28. S.M. Eich, M. Kasprzak, A. Gusak, and G. Schmitz: *Acta Mater.*, 2012, vol. 60, pp. 3469–79.
29. I. Kaur, Y. Mishin, and W. Gust: *Fundamentals of Grain and Interphase Boundary Diffusion*, 3rd ed., Wiley publishers, New York, 1995, pp. 343–49.
30. B. Wierzba and W. Skibinski: *J. Alloys Compds.*, 2016, vol. 687, pp. 104–08.

Publisher's Note Springer Nature remains neutral with regard to jurisdictional claims in published maps and institutional affiliations.